

**Hardness tests used to establish
constitutive models**

John F. Moxnes and Øyvind Frøyland

FFI/RAPPORT-2006/02802

FORSVARETS FORSKNINGSINSTITUTT
Norwegian Defence Research Establishment
P O Box 25, NO-2027 Kjeller, Norway

1) PUBL/REPORT NUMBER FFI/RAPPORT-2006/02802	2) SECURITY CLASSIFICATION UNCLASSIFIED	3) NUMBER OF PAGES 35
1a) PROJECT REFERENCE FFI-V/1072/01	2a) DECLASSIFICATION/DOWNGRADING SCHEDULE -	
4) TITLE Hardness tests used to establish constitutive models		
5) NAMES OF AUTHOR(S) IN FULL (surname first) Moxnes John F., Frøyland Øyvind		
6) DISTRIBUTION STATEMENT Approved for public release. Distribution unlimited. (Offentlig tilgjengelig)		
7) INDEXING TERMS IN ENGLISH:		
a) <u>Hardness</u>	IN NORWEGIAN:	
b) <u>Cavity Theory</u>	a) <u>Hardhet</u>	
c) <u>Material models</u>	b) <u>Kavitetsteori</u>	
d) <u>Indentation</u>	c) <u>Materialmodeller</u>	
e) <u>Experimental</u>	d) <u>Innpressing</u>	
	e) <u>Eksperimentell</u>	
THESAURUS REFERENCE:		
8) ABSTRACT		
<p>In this report a study of the hardness of different materials are performed theoretically and experimentally. The objective was to study whether the hardness test could be used to establish constitutive material models.</p> <p>We apply the famous cavity theory for rigid penetration for the hardness test, and expand the theory to include compressibility and strain hardening.</p> <p>We found discrepancies between the results from cavity theory and the experimental results. Contrary to the theory, the hardness is dependent on the form of the penetrator. Also the cavity theory overestimates the hardness with approximately 20% for the steel specimen and the Wolfram Carbide specimen. In general we show that material data from the hardness test can be used as an important input to construction of constitutive material models.</p>		
9) DATE 2008-01-15	AUTHORIZED BY This page only Bjarne Haugstad	POSITION Director of Research

CONTENTS

		Page
1	INTRODUCTION	7
2	THE STATIC CAVITY THEORY	8
3	THE EXPERIMENTAL SETUP	15
4	HARDNESS TEST OF WOLFRAM CARBIDE HARDCORES	16
5	HARDNESS TEST OF ARMOX 370 STEEL	24
6	HARDNESS TEST OF THE HUMAN SKULL	26
7	HARDNESS TEST OF JACKETS OF PROJECTILES	26
8	CONCLUSION/DISCUSSION	28

Hardness tests used to establish constitutive models

1 INTRODUCTION

Good material models are necessary requisites for applying computer simulations. To achieve predictability of these mathematical material models, they are usually tuned to experimental data from tests very different from the actual set up for a specific computer simulation. The reason for this procedure is that most material models have many free parameters, which always can be tuned to match a specific problem. By establishing material data from one type of test, and achieving good simulation results for very different types of tests, good credibility of material models are achieved.

Typical scientific tests for establishing constitutive models are the simple compression test, the bending test, the unilateral compression test and the split Hopkinson bar test. Extensive engineering use is made of the hardness test. The hardness is simply the resistance of a material to plastic deformation. The test is very simple to make, it is quick, and requires only a small specimen. The only specification for the test specimen is that there is at least one plane surface. On the other hand, hardness measurements have only rarely been employed in scientific studies because of the objections that the hardness test involves a complex state of stress, and that it measures not one but several properties [3]. A relationship between hardness and yield point has been shown in reference [9]. A linear relation between tensile strength and the Brinell hardness of quenched and tempered alloys of steel has been found in reference [10]. The hardness is in close correlation with the fundamental atomic and crystalline properties [4-7]. Relations have been found between the hardness of pure metals and their compressibility and temperature [1,2,8].

On the continuum level analytical relations between the hardness and the main parameters of a constitutive model is difficult to achieve unless the material is assumed to be perfect elastic/plastic and incompressible. During the hardness test the pressure/von Mises-stress fraction is much larger than for most other compression/tension tests. This is of special importance for brittle materials since the yield stress and the fracture stress are strongly dependent on the pressure.

Of large interest for the MP ammunition is the ability to simulate penetration of hard cores of Wolfram Carbide into different targets. We have earlier presented a material model constructed on data from the compression and bending tests [11-13].

This study starts by revising the results from a newly developed exact analytical theory for the spherical cavity expansion for incompressible materials. The theory is based on the cavity theory for penetration. Thereafter the theory is expanded to include compressibility and strain hardening. The theory is then applied to hardness measurements of materials that strain harden.

We apply hardness tests on Wolfram Carbide, steel, human bones and brass jackets of 12.7 mm projectiles. We show experimentally that the indentation forces have to be above a certain value in order to achieve constant hardness for a given indenter and a given material. This level is increasing with the hardness of the material. Below the critical value the hardness is dependent on the applied force. We also show experimentally that the hardness depends somewhat on the form of the indenter. This last experimental result is in disagreement with the main assumption of the cavity theory.

Of special interest is also whether in situ hardness measurements can be used as quality check of materials. This is of special importance for hardmetals and ceramic materials, which are due to processing difficulties causing inhomogeneity of the material.

In general we show that material data from the hardness tests are important inputs to constitutive models.

2 THE STATIC CAVITY THEORY

The cavity theory gives for an expanding spherical cavity the following radial stress and pressure for a spherical cavity in an infinite material when using the stationary equation of motion

$$\begin{aligned}\sigma_r(r,t) &= \int_r^\infty \frac{2(\sigma_r(r',t) - \sigma_\theta(r',t))}{r'} dr', r \geq S(t) \\ p(r,t) &\stackrel{def}{=} -\frac{1}{3}(\sigma_r + \sigma_\theta + \sigma_\phi) = -\frac{1}{3}(\sigma_r + 2\sigma_\theta), \sigma_\theta = \sigma_\phi\end{aligned}\tag{2.1}$$

where $S(t)$ is the inner radius of the spherical cavity as a function of time, p is the pressure and σ_r is the radial stress and σ_θ is the circumferential stress. Symmetry gives when assuming a von Mises material that

$$\sigma_r - \sigma_\theta = -\text{von Mises stress} \leq 0,\tag{2.2}$$

From the spherical symmetry it follows from the material conservation that

$$\begin{aligned}r &\stackrel{def}{=} r_0 + u(r,t) \\ 4\pi r_0^2 dr_0 \rho_0 &\stackrel{mod}{=} 4\pi r^2 dr \rho \Rightarrow \frac{\partial}{\partial r} \left[(r - u(r,t))^3 \right] = 3r^2 (\rho / \rho_0)\end{aligned}\tag{2.3}$$

where $u(r,t)$ is the displacement, r_0 is the Lagrangian radial coordinate and r is Eulerian radial coordinate. ρ_0 is the initial density and ρ is the current density. The boundary condition is $u(S(t),t) = S(t)$, where $S(t)$ is the position of the inner surface. Equation (2.3) is easily solved when assuming the incompressibility relation $\rho_0 = \rho$. It follows from (2.3) that

$$u(r, t) = r \left[1 - \left(1 + \frac{a^3 - S(t)^3}{r^3} \right)^{1/3} \right], u(S(t), t) = S(t) - a \quad (2.4)$$

where a is the initial hole radius of the cavity. From (2.4), the definition and the spherical symmetry the radial velocity follows as

$$\frac{\partial u}{\partial t} + v \left(\frac{\partial u}{\partial r} \right) \stackrel{def}{=} v \Rightarrow v = \frac{\partial u / \partial t}{1 - \partial u / \partial r} = \frac{V(t)S(t)^2}{r^2} \quad (2.5)$$

where $V(t) = \dot{S}(t)$ is the radial velocity of the inner surface (assumed to be quasi-static).

In addition, the logarithmic strains follow from the definition, equation (2.4) and the spherical symmetry, to read

$$\begin{aligned} \varepsilon_r &\stackrel{def}{=} -\text{Ln}(1 - \partial u / \partial r) = \frac{2}{3} \text{Ln} \left(1 + \frac{a^3 - S(t)^3}{r^3} \right) \\ \varepsilon_\theta &\stackrel{def}{=} -\text{Ln}(1 - u / r) = \varepsilon_\phi = -\frac{1}{3} \text{Ln} \left(1 + \frac{a^3 - S(t)^3}{r^3} \right) = -\frac{1}{2} \varepsilon_r \end{aligned} \quad (2.6)$$

Inserting (2.4) and (2.5) into (2.6) gives directly that

$$\frac{D\varepsilon_r}{dt} = \frac{\partial \varepsilon_r}{\partial t} + v \frac{\partial \varepsilon_r}{\partial r} = \frac{\partial v}{\partial r}, \frac{D\varepsilon_\theta}{dt} = \frac{\partial \varepsilon_\theta}{\partial t} + v \frac{\partial \varepsilon_\theta}{\partial r} = \frac{v}{r} \quad (2.7)$$

which show that by applying spherical symmetry the strain rates are given as the total derivative of the logarithmic strain. Moreover the reduced strains are given by

$$\begin{aligned} e_r &\stackrel{def}{=} \varepsilon_r - (1/3)(\varepsilon_r + \varepsilon_\theta + \varepsilon_\phi) = \varepsilon_r, e_\theta = \varepsilon_r = -\frac{1}{2} e_r \\ e_{eff} &\stackrel{def}{=} \left(\frac{2}{3} e_{ij}^2 \right)^{1/2} = -e_r, \end{aligned} \quad (2.8)$$

By applying a material model where von Mises = $M(e_{eff})$, the integration (2.1) can be performed to give the radial stress and the pressure if the strains are inserted. Consider the specific test example

$$\text{Mis}(e_{eff}) \stackrel{mod}{=} Y \left(1 - \text{Exp}(-e_{eff} 3G / Y) \right), Y = \text{const.} G = \text{const.} \quad (2.9)$$

where Y is the ultimate plastic stress, and G is the shear modulus. Inserting the strains in (2.6) into (2.2) and (2.9) gives that

$$\sigma_r - \sigma_\theta = -\text{Mis}(e_{\text{eff}}) = -Y \left[1 - \text{Exp} \left(\text{Ln} \left[\left(1 + \frac{a^3 - S(t)^3}{r^3} \right)^{2G/Y} \right] \right) \right] = -Y \left(1 - \left(1 + \frac{a^3 - S(t)^3}{r^3} \right)^{2G/Y} \right) \quad (2.10)$$

Inserting (2.10) into (2.1) gives the radial stress as

$$\sigma_r(r, t) = \int_r^\infty \frac{-2Y \left(1 - \left(1 + \frac{a^3 - S(t)^3}{r'^3} \right)^{2G/Y} \right)}{r'} dr', S(t) \geq a \quad (2.11)$$

$$p(r, t) = -\frac{1}{3}(\sigma_r + 2\sigma_\theta) = -\sigma_r(r, t) - \frac{2}{3}\text{Mis}(e_{\text{eff}})$$

Thus at the inner cavity surface $r = S(t)$

$$\sigma_r(S(t), t) = \int_{S(t)}^\infty \frac{-2Y \left(1 - \left(1 + \frac{a^3 - S(t)^3}{r'^3} \right)^{2G/Y} \right)}{r'} dr' \quad (2.12)$$

Substituting that $1 + (a^3 - S(t)^3)/r'^3 = u$ gives that

$$\begin{aligned} \sigma_r(S(t), t) &= -\frac{2Y}{3} \int_{a^3/S(t)^3}^1 \left(\frac{1-u^{2G/Y}}{1-u} \right) du \\ \text{Lim}_{a^3/S(t)^3 \rightarrow 0} \sigma_r(S(t), t) &= -\frac{2Y}{3} \text{HarmonicNumber} \left(\frac{2G}{Y} \right), \\ p(S(t), t) &= -\sigma_r(S(t), t) - \frac{2}{3}\text{Mis}(e_{\text{eff}}) = \frac{2Y}{3} \int_{a^3/S(t)^3}^1 \left(\frac{1-u^{2G/Y}}{1-u} \right) du - \frac{2Y}{3} \left(1 - \left(\frac{a^3}{S(t)^3} \right)^{2G/Y} \right) \\ \text{Lim}_{a^3/S(t)^3 \rightarrow 0} p(S(t), t) &= \frac{2Y}{3} \text{HarmonicNumber} \left(\frac{2G}{Y} \right) - \frac{2Y}{3} \end{aligned} \quad (2.13)$$

Observe from (2.13) that the radial stress at the inner surface is independent of the cavity radius $S(t)$, although the material model strain hardens, when the initial radius of the cavity hole goes to zero.

Assume a linear elastic/plastic material. In the elastic region we have

$$\begin{aligned} \sigma_r &= \frac{E}{(1+\nu)(1-2\nu)} ((1-\nu)\varepsilon_r + 2\nu\varepsilon_\theta), \sigma_\theta = \frac{E}{(1+\nu)(1-2\nu)} (\nu\varepsilon_r + \varepsilon_\theta) \\ \sigma_r - \sigma_\theta &= \frac{E}{(1+\nu)} (\varepsilon_r - \varepsilon_\theta) = 2G(e_r - e_\theta) = 3Ge_r \end{aligned} \quad (2.14)$$

For the plastic region we state the conventional Mises relation. Thus the following model is applied for an ideal elastic/plastic material

$$\begin{aligned}
Mis(e_{eff}) &= 3Ge_{eff} \text{ when } e_{eff} \leq \frac{Y}{3G} \\
Mis(e_{eff}) &= Y \text{ when } e_{eff} \geq \frac{Y}{3G}
\end{aligned} \tag{2.15}$$

Further, denote the elastic/plastic interface by $r = s(t)$, thus the position of this interface follows from (2.6) and (2.15) as

$$3Ge_{eff} = Y \Leftrightarrow -2G \operatorname{Ln} \left(1 + \frac{a^3 - S(t)^3}{s(t)^3} \right) = Y \Leftrightarrow s(t) = \frac{S(t) \left(1 - a^3 / S(t)^3 \right)^{1/3}}{\left(1 - \operatorname{Exp} \left(-\frac{Y}{2G} \right) \right)^{1/3}} \tag{2.16}$$

$$s(t) \approx \left(\frac{2G}{Y} \right)^{1/3} S(t) \text{ when } \frac{Y}{2G} \ll 1 \text{ and } \frac{a^3}{S(t)^3} \ll 1$$

Only the approximate solutions are known from the literature. Observe that the position of the plastic surface is proportional with the position of the inner surface of the cavity for large radii compared to the initial radius. Plastic flow starts instantaneously at the inner surface and moves ahead of the inner surface. At the inner surface $r = S(t)$, we get from (2.1), (2.2) and (2.16) the stress

$$\begin{aligned}
\sigma_r(S(t), t) &= - \int_{S(t)}^{s(t)} \frac{2Y \left(1 - \left(\frac{a^3}{S(t)^3} \right)^{2G/Y} \right)}{r'} dr' + \int_{s(t)}^{\infty} \left(\frac{4G \operatorname{Ln} \left(1 + \frac{a^3 - S(t)^3}{r'^3} \right)}{r'} \right) dr', \\
&= -2Y \left(1 - \left(\frac{a^3}{S(t)^3} \right)^{2G/Y} \right) \operatorname{Ln} \left(\frac{s(t)}{S(t)} \right) - \frac{4G}{3} \int_{\left(1 - \operatorname{Exp} \left(\frac{-Y}{2G} \right) \right)^{1/3} \left(1 - \frac{a^3}{S(t)^3} \right)^{-1/3}}^0 \frac{\operatorname{Ln}(1-u)}{u} du \\
&= \frac{2Y}{3} \left(1 - \left(\frac{a^3}{S(t)^3} \right)^{2G/Y} \right) \operatorname{Ln} \left(\frac{1 - \operatorname{Exp} \left(\frac{-Y}{2G} \right)}{1 - \frac{a^3}{S(t)^3}} \right) - \frac{4G}{3} \operatorname{Li}_2 \left(\frac{\left(1 - \operatorname{Exp} \left(\frac{-Y}{2G} \right) \right)^{1/3}}{1 - \frac{a^3}{S(t)^3}} \right) \\
&\approx -\frac{2Y}{3} \left(1 - \left(\frac{a^3}{S(t)^3} \right)^{2G/Y} \right) \operatorname{Ln} \left(\frac{2G}{Y \left(1 - \frac{a^3}{S(t)^3} \right)} \right) - \frac{2Y}{3} + \frac{1}{4} \frac{Y^2}{3G} + \dots \text{ when } \frac{Y}{2G} \ll 1
\end{aligned} \tag{2.17}$$

where $Li_2()$ is the Jonquieres function of second order.

The hardness is defined as the force on a penetrator divided with the projected contact area along the axis of the penetrator.

According to the cavity theory applied to indentation of rigid penetrators, the axial force on the penetrator is equal to the radial stress from the spherical cavity theory times the projected contact area. Using this theory together with the definition of the hardness we achieve that theoretically the hardness H should be given as

$$H(x) \stackrel{def}{=} F(x) / A(x) \stackrel{mod}{=} \sigma_r(S(t), t) A(x) / A(x) = \sigma_r(S(t), t) = const. \quad (2.18)$$

where F is the force, x is the indentation distance and $A(x)$ is the projected contact area. Thus the hardness for a given material is theoretically given as the radial stress calculated from the spherical cavity theory. Thus the hardness becomes independent of the indentation distance for large cavities and in general independent of the form of the nose of the indenter. Experiments below will show that the hardness is indeed dependent on the form of the penetrator.

Experiments below also show that the hardness tends to decrease for small indentation forces or distances. The reason for this, we believe, is that during the initial phase of the indentation the cavity is far from spherical.

Assume for simplicity that the material behaves linearly elastic. The radius, a , of contact between a sphere of radius R and a flat surface is according to the Hertzian solution given by

$$a = \left(\frac{3}{4}\right)^{1/3} \frac{F^{1/3} R^{1/3}}{E^{1/3}} (1 - \sigma^2)^{1/3}, \quad \frac{a}{R} = \left(\frac{3}{4}\right)^{1/3} \frac{F^{1/3}}{E^{1/3} R^{2/3}} (1 - \sigma^2)^{1/3} \quad (2.19)$$

where E is the Young's modulus, F is the force and σ is the Poisson ratio. The force per projected contact area (the hardness) then becomes

$$H = \frac{F}{\pi a^2} = \frac{1}{\pi} \left(\frac{4E}{3R(1 - \sigma^2)} \right)^{2/3} F^{1/3} = \frac{4E}{3\pi(1 - \sigma^2)} \frac{a}{R}, \quad (2.20)$$

Thus it follows that the hardness is inversely proportional with the radius of the spherical indenter or proportional with the force raised to the power of 1/3. Also the force is linearly dependent of the radius of the contact area.

The necessary force (or the indentation distance) to reach the prediction of the cavity theory is uncertain. First of all the linearity in the Hertzian solution ceases to be valid for some penetration distance. To account for this, we first renormalizes (2.20), hopefully to be valid for large strains. Our suggestion is

$$H = \frac{F}{\pi a^2} = \frac{4}{3\pi(1 - \sigma^2)} Mis \left(\frac{a}{R} \right), \quad (2.21)$$

where Mis is again the von Mises stress. Totally we suggest that

$$H = \text{Min} \left(\frac{4}{3\pi(1-\sigma^2)} M \left(\frac{a}{R} \right), \text{Cavity theory} \right) \quad (2.22)$$

In general we expect that when the fraction a/R becomes large, the cavity prediction is reached. Thus the indentation distance should be above a certain value. This value is dependent of the hardness of the material. A hard material needs large forces to achieve the minimum indentation distance.

The cavity theory is in the literature based on the incompressibility assumption. We now consider a compressible material and expand the theory accordingly. The equation of state is as an example assumed to be given by

$$p = K(\rho/\rho_0 - 1) \quad (2.23)$$

where K is the bulk modulus. Inserting into the material conservation equation (2.3) gives that the density can be eliminated, to read

$$\frac{\partial}{\partial r} \left[(r - u(r, t))^3 \right] = 3r^2 (1 + p/K) \Rightarrow u(r, t) = r - \left[\int_{S(t)}^r 3u^2 (1 + p(u)/K) \right]^{1/3} du \quad (2.24)$$

when we assume large cavity holes compared to the initial hole. The reduced effective strain to be inserted when the material is compressible, is necessary. Our basic assumption is that the *volumetric change is small* (not necessary small strains). Let

$$\rho/\rho_0 - 1 \approx -(\varepsilon_r + 2\varepsilon_\theta) \quad (2.25)$$

It then follows from (2.24) and (2.26) and the definitions that

$$e_{eff} = -e_r = -(\varepsilon_r - (1/3)(\varepsilon_r + 2\varepsilon_\theta)) \approx -\varepsilon_r - p/(3K) \quad (2.26)$$

According to the definition $\varepsilon_r = -\text{Ln}(1 - \partial u / \partial r)$. It follows from (2.24) that

$$\varepsilon_r = -\text{Ln} \left(1 - \frac{\partial u(r, t)}{\partial r} \right) = -\text{Ln} \left(\frac{r^2 (1 + p(r)/K)}{\left[\int_{S(t)}^r 3u^2 (1 + p(u)/K) du \right]^{2/3}} \right) \quad (2.27)$$

Thus we have from (2.26), (2.27) that

$$\begin{aligned}
e_{eff} &= \text{Ln} \left(\frac{r^2 (1 + \lambda p(r)/K)}{\left[\int_{S(t)}^r 3 u^2 (1 + \lambda p(u)/K) du \right]^{2/3}} \right) - \lambda \frac{P}{3K} \\
&\approx \text{Ln} \left(\frac{r^2}{\left[\int_{S(t)}^r 3 u^2 du \right]^{2/3}} + \frac{r^2 (\lambda p(r)/K)}{\left[\int_{S(t)}^r 3 u^2 du \right]^{2/3}} - 2r^2 \int_{S(t)}^r \frac{u^2 \lambda p(u)}{K \left[\int_{S(t)}^r 3 u^2 du \right]^{5/3}} du \right) - \lambda \frac{P}{3K} \\
&= \text{Ln} \left(\left(1 - S^3 / r^3 \right)^{-2/3} \left(1 + \lambda p(r)/K - \lambda \frac{2 \int_{S(t)}^r u^2 p(u) du}{K r^3 (1 - S^3 / r^3)} \right) \right) - \lambda \frac{P}{3K} \\
&\approx -\frac{2}{3} \text{Ln} \left(1 - S^3 / r^3 \right) + \frac{\lambda p(r)}{K} - \lambda \frac{2 \int_{S(t)}^r u^2 p(u) du}{K r^3 (1 - S^3 / r^3)} - \lambda \frac{P}{3K} \left[\int_{S(t)}^r 3 u^2 du \right]^{2/3} \\
&\approx -\frac{2}{3} \text{Ln} \left(1 - S^3 / r^3 \right), \text{ when } \frac{2 \int_{S(t)}^r u^2 p(u) du}{K r^3 (1 - S^3 / r^3)} \approx \frac{2P}{3K}
\end{aligned} \tag{2.28}$$

Here λ is a parameter that is equal to one or zero, depending on whether the compressibility is to be accounted for. Equation (2.28) has to be solved together with equations (2.1) and (2.2), to read

$$\begin{aligned}
\sigma_r(r,t) &= -\int_r^\infty \frac{2\text{Mis}(e_{eff}(u))}{u} du, r \geq S(t), (a) \\
e_{eff}(r,t) &= -\frac{2}{3} \text{Ln} \left(1 - S^3 / r^3 \right) + \frac{\lambda p(r)}{K} - \lambda \frac{2 \int_{S(t)}^r u^2 p(u) du}{K r^3 (1 - S^3 / r^3)} - \lambda \frac{P}{3K} (b) \\
p(r,t) &= -\frac{1}{3} (\sigma_r + 2\sigma_\theta) = -\frac{1}{3} (3\sigma_r + 2\text{Mis}(e_{eff})), (c)
\end{aligned} \tag{2.29}$$

Equation (2.29) is solved by iteration. First, only the first term on the right hand side in (2.29b) is used for the effective reduced plastic stain. The corresponding radial stress is calculated when inserting into equation (2.29a). The pressure is then calculated according to (2.29c). Thereafter, for the next approximation, the reduced effective plastic strain is found by inserting the radial stress into (2.29b). The next approximation for the radial stress is calculated by inserting into (2.29a), etc. In the next section the solution of (2.29) was achieved numerically and is compared with the experimental results of the hardness. The von Mises function as a function of reduced strain and the elastic constants were input to the numerical calculations. The simple tension or compression tests have earlier been used to develop the von Mises function.

3 THE EXPERIMENTAL SETUP

For the hardness measurement three different diamond indenters were used:

- A conical indenter (Rockwell indenter) with an angle of 120° .
- A pyramidal indenter (Vickers indenter) with an angle of 136° between the faces.
- A pyramidal indenter (custom fabrication) with an angle of 90° between the faces.

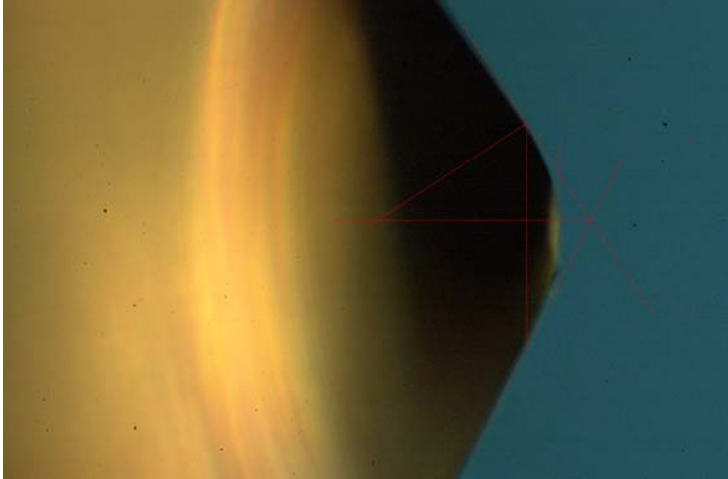


Figure 3.1: Conical indenter.

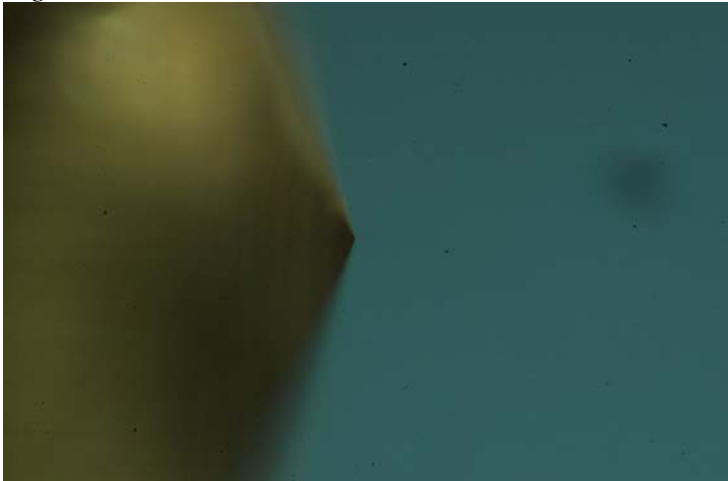


Figure 3.2: Pyramidal indenter (136°)

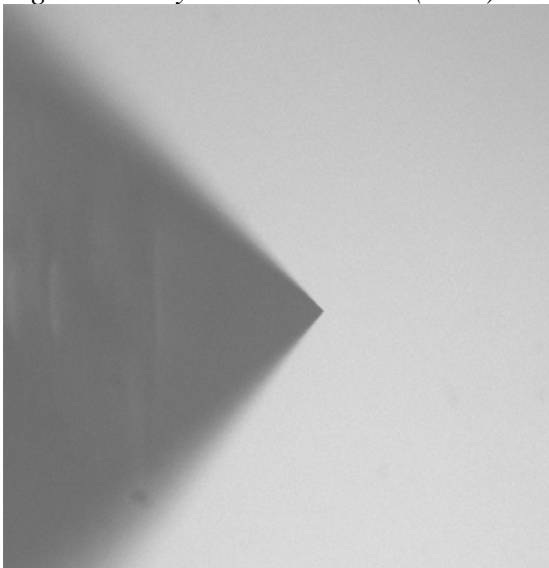


Figure 3.3: Pyramidal indenter (90°)

4 HARDNESS TEST OF WOLFRAM CARBIDE HARDCORES

The hardness of a specimen of Wolfram Carbide was examined. Different approaches were performed. The form of the indenter and the force were varied. Also the surface of the specimen was handled differently.

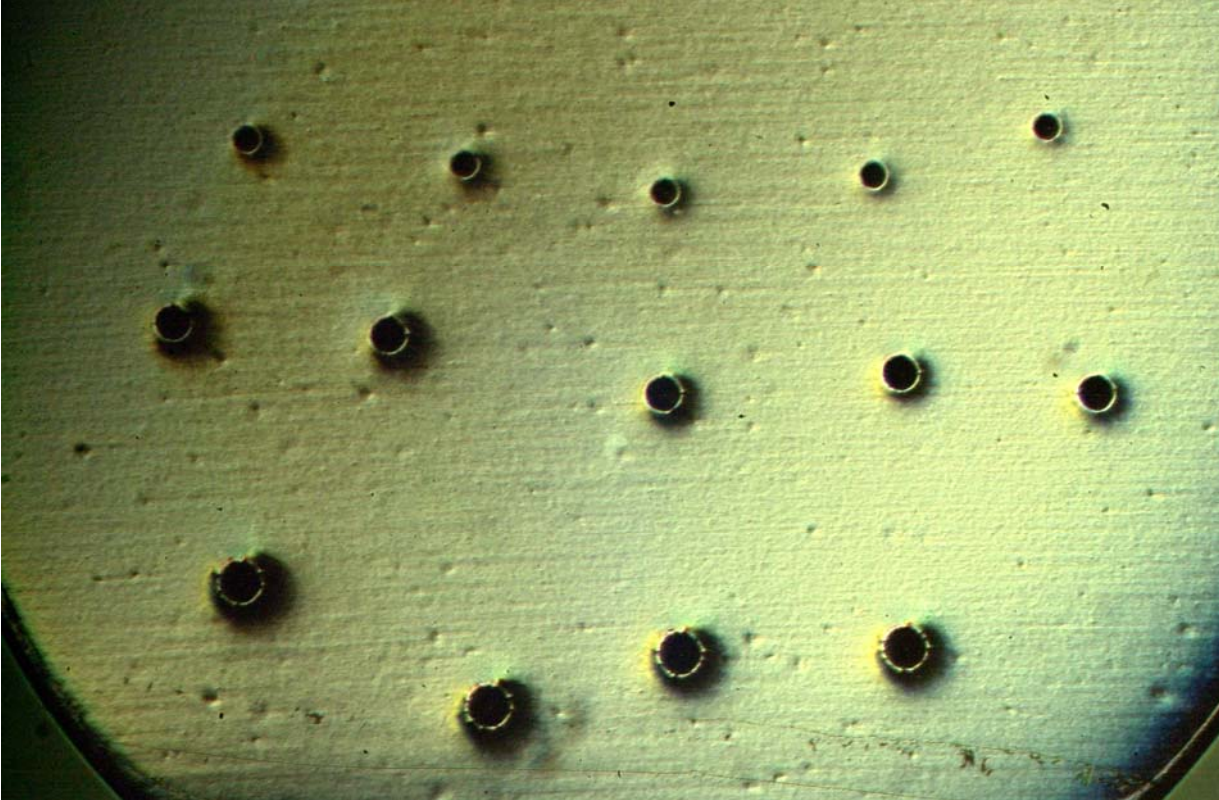


Figure 4.1: The indentations in a specimen of Wolfram Carbide (G15) using a conical indenter at different loads.

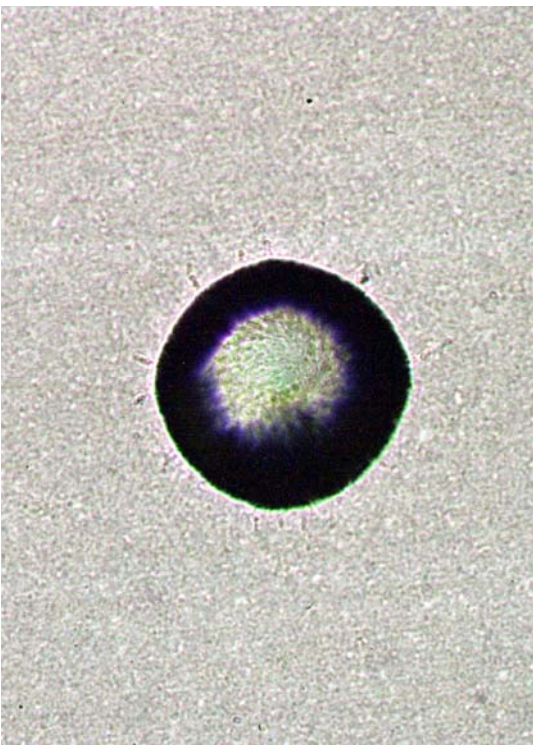


Figure 4.2: Indentation in Wolfram Carbide (G15). Conical indenter. Load 30 kg.

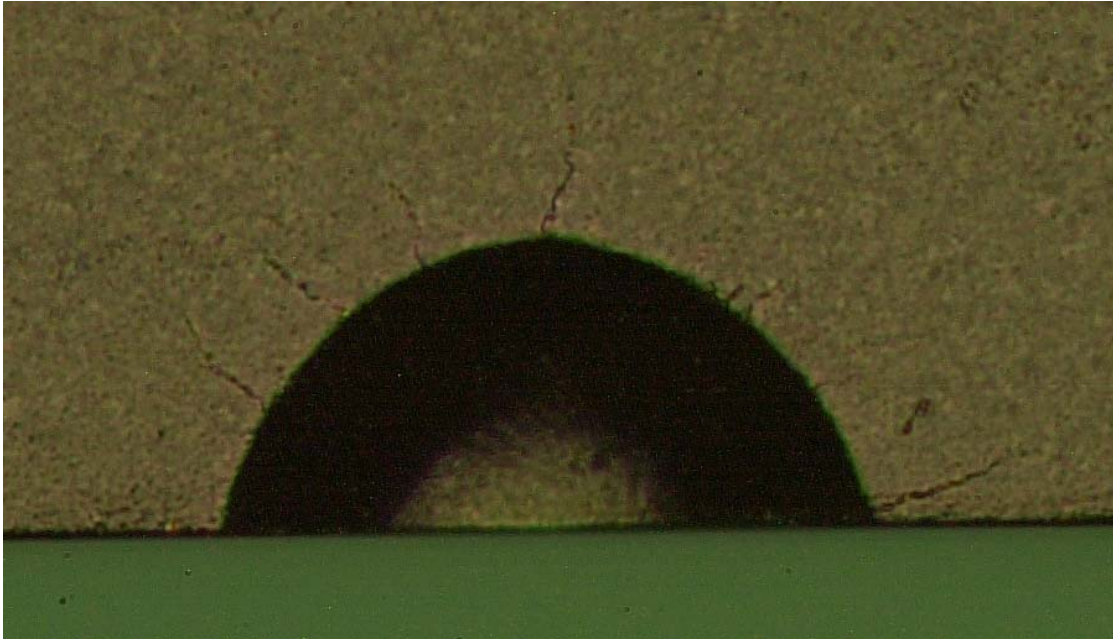


Figure 4.3: Close up of a split indentation hole in Wolfram Carbide (G15). Conical indenter. Load 45 kg.



Figure 4.4: The indentation hole in Figure 3.4 seen from the side.

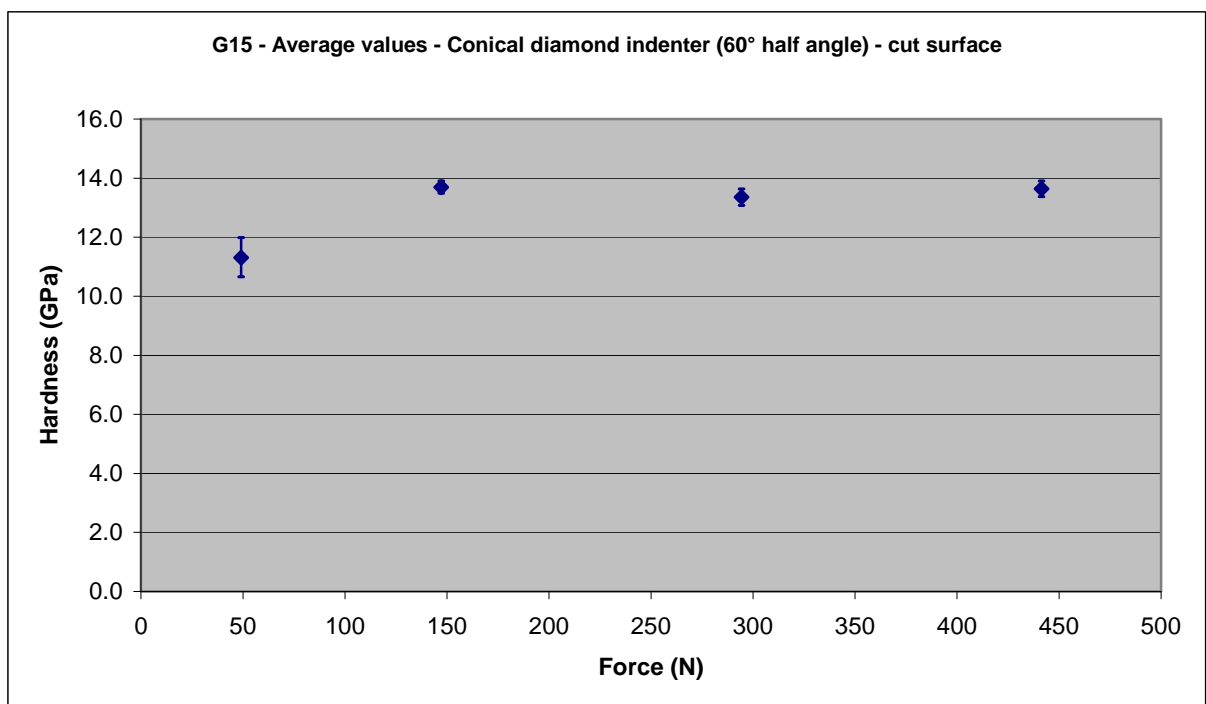


Figure 4.5: The measured hardness for different forces with a conical indenter.

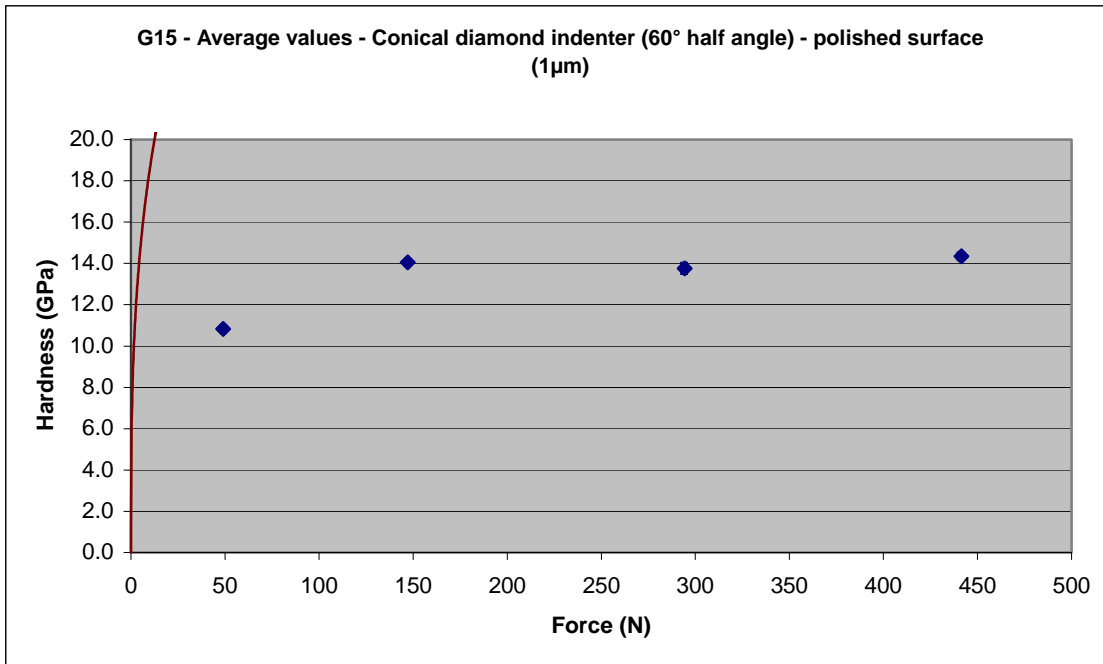
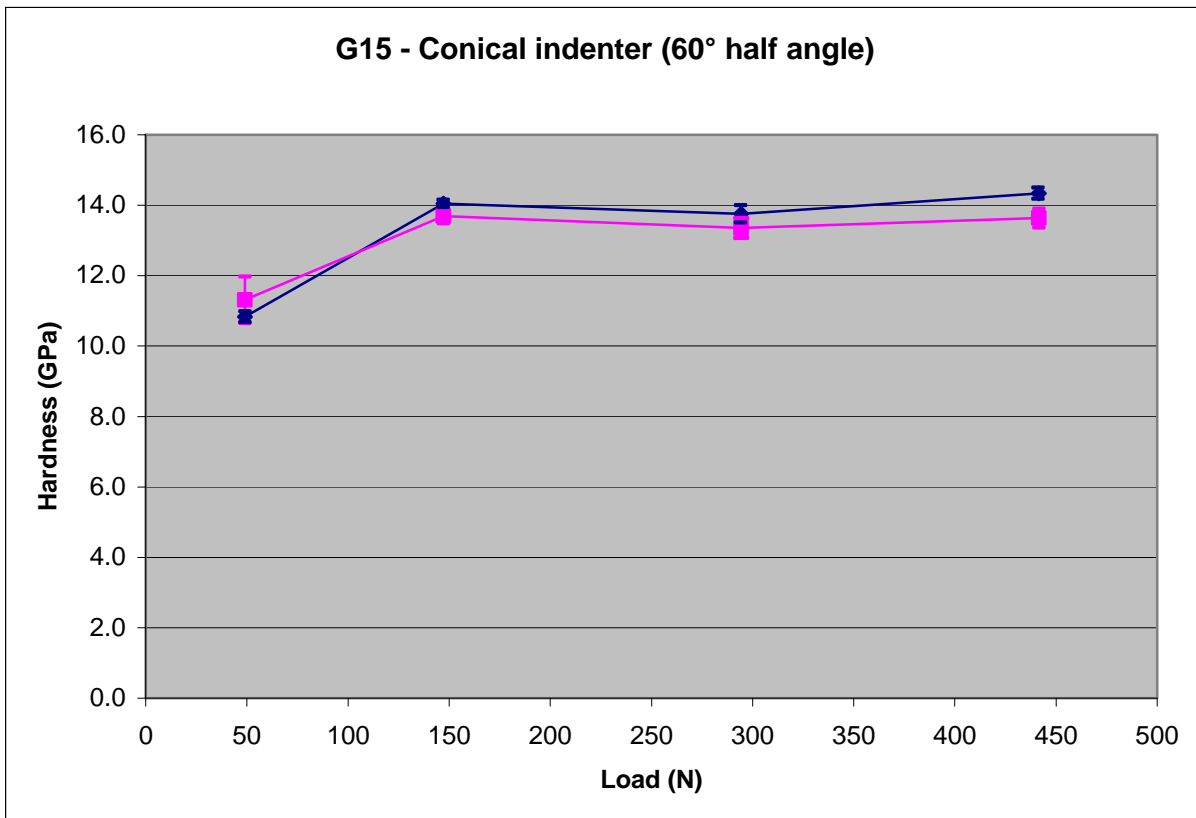


Figure 4.6: Analytical and experimental values. The function is equation (2.20).



◆ Polished surface (1 µm) ■ Cut surface

Figure 4.7: The measured hardness for a specimen with a polished surface and a cut surface with conical indenter.

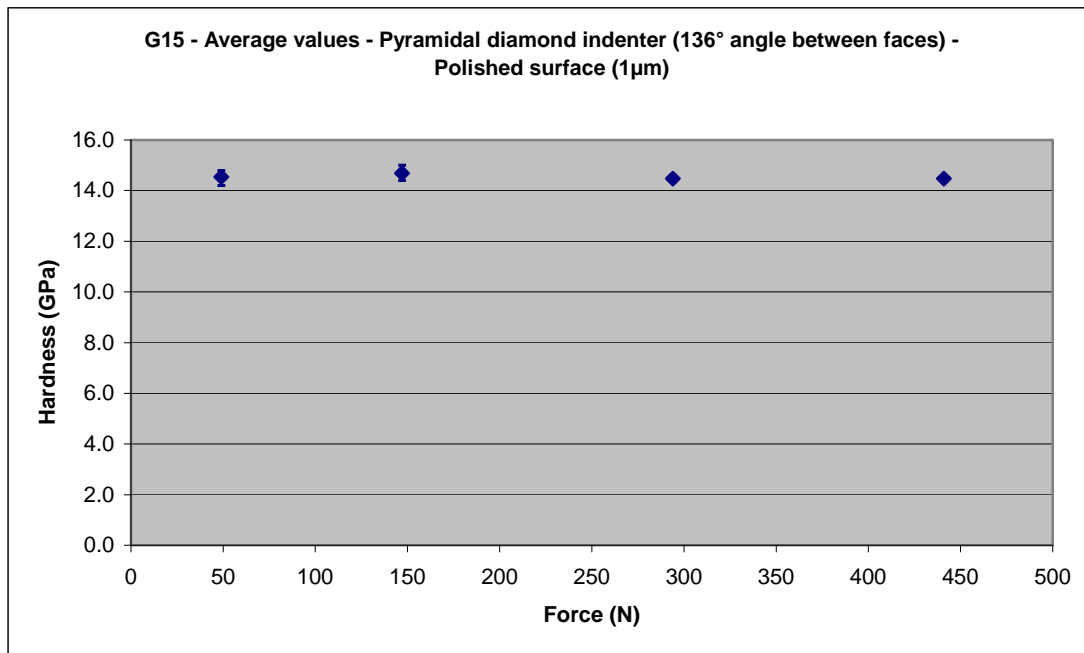
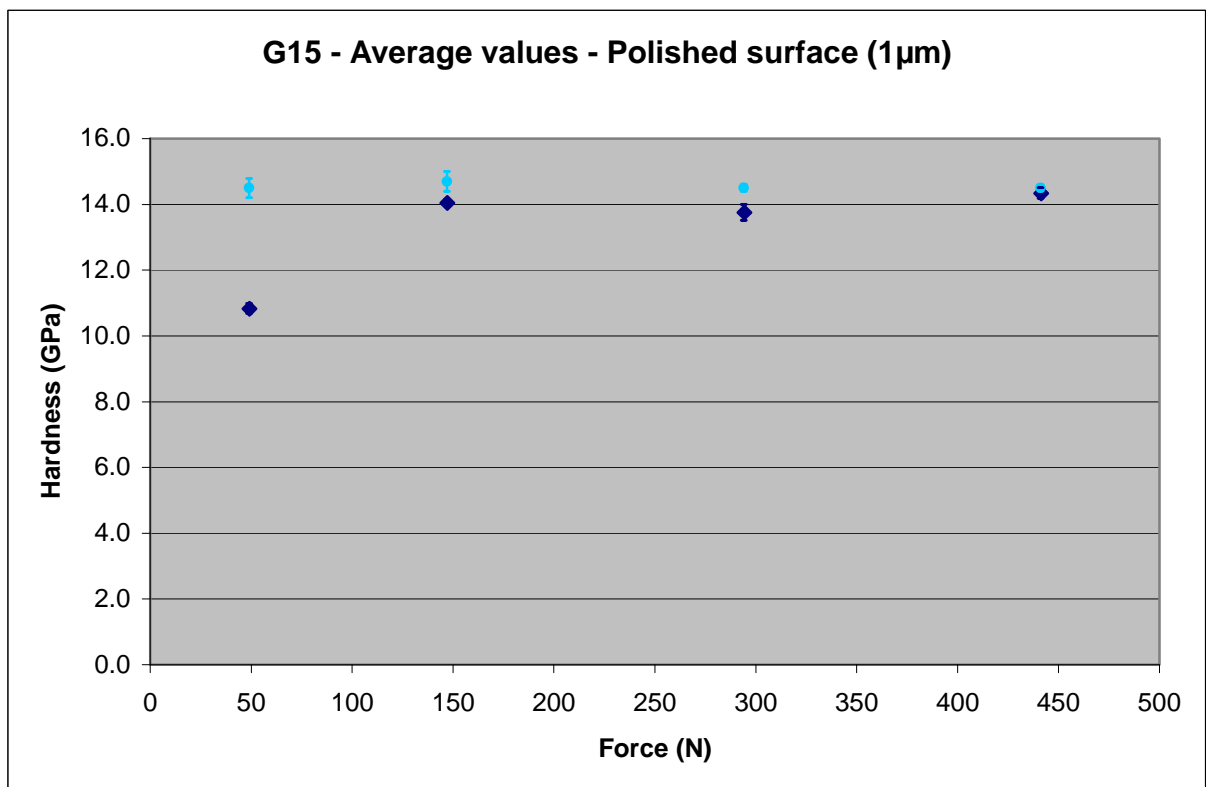
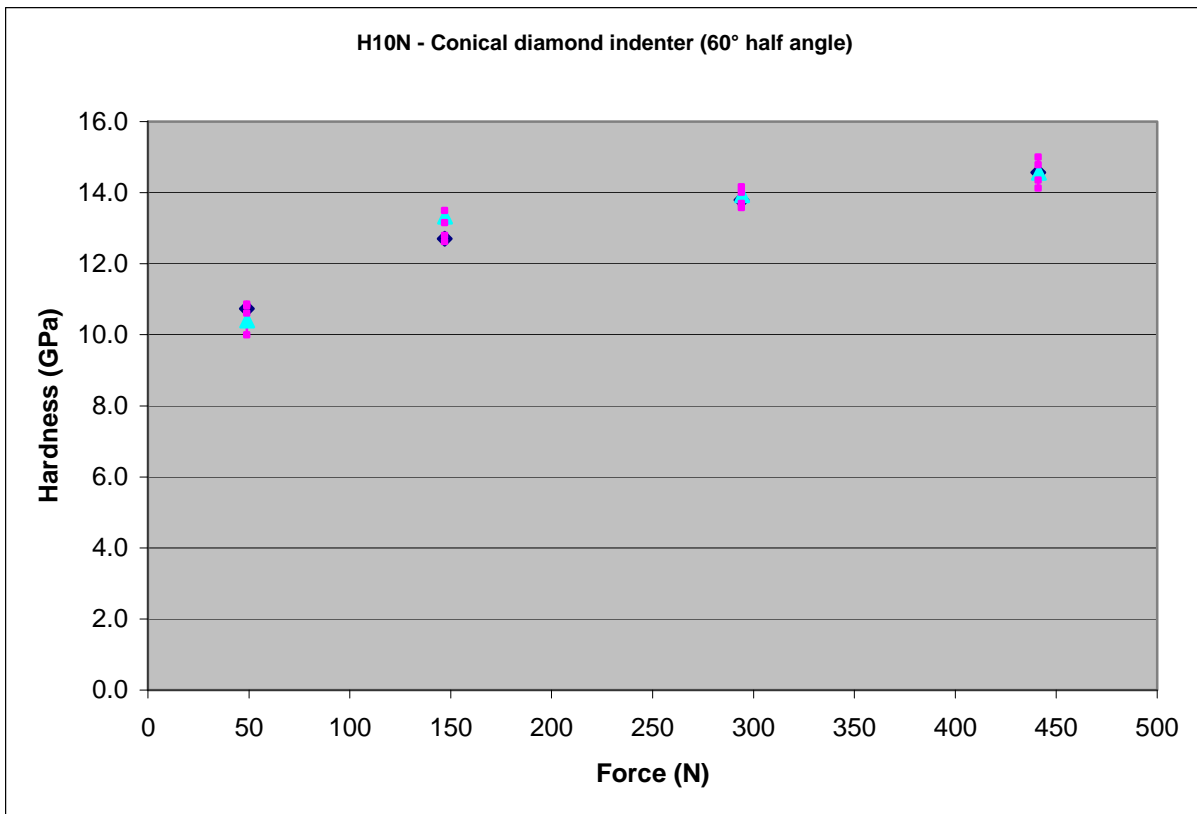


Figure 4.8: The measured hardness of G15 for different forces when using the pyramidal indenter.



◆ Conical (120°) indenter ● Pyramide (136°) indenter

Figure 4.9: The measured hardness for the conical and the pyramidal indenter from Figure 4.6 and 4.8.



◆ Polished surface (1 μm) ▲ Cut surface

Figure 4.10: The measured hardness for a specimen with a polished surface and a cut surface with conical indenter.

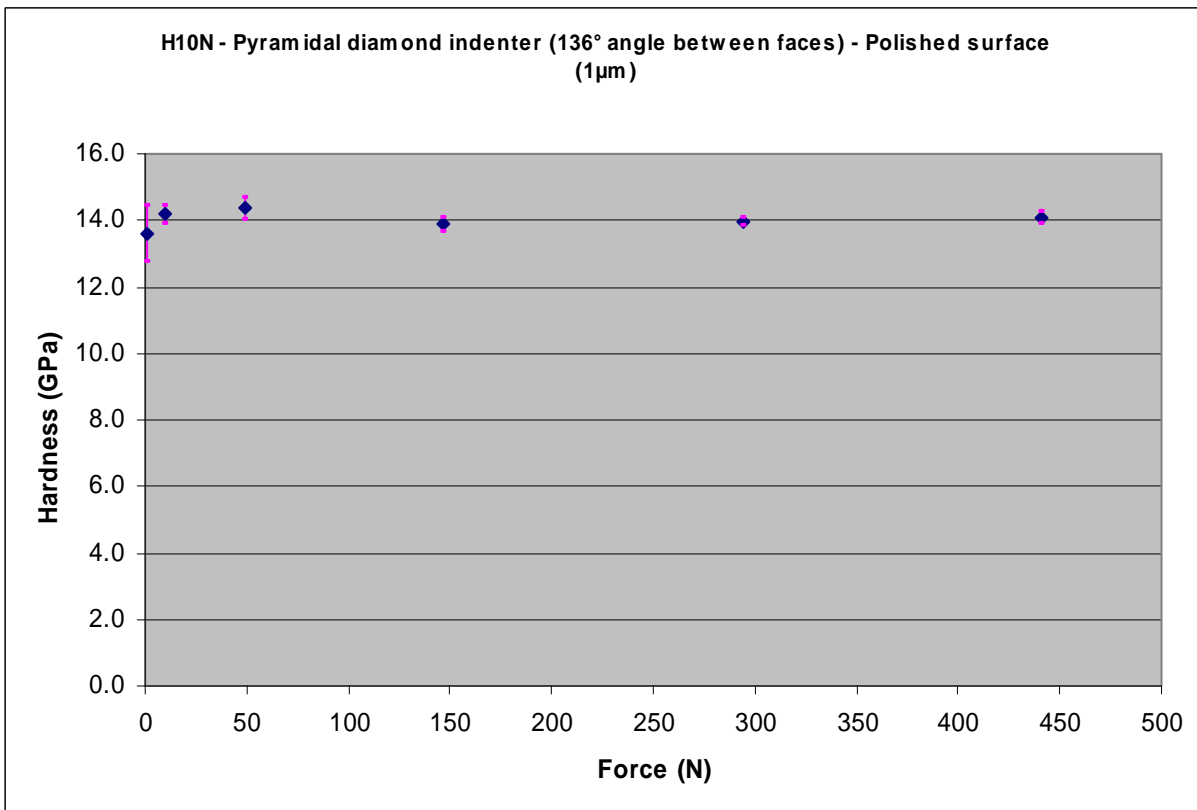
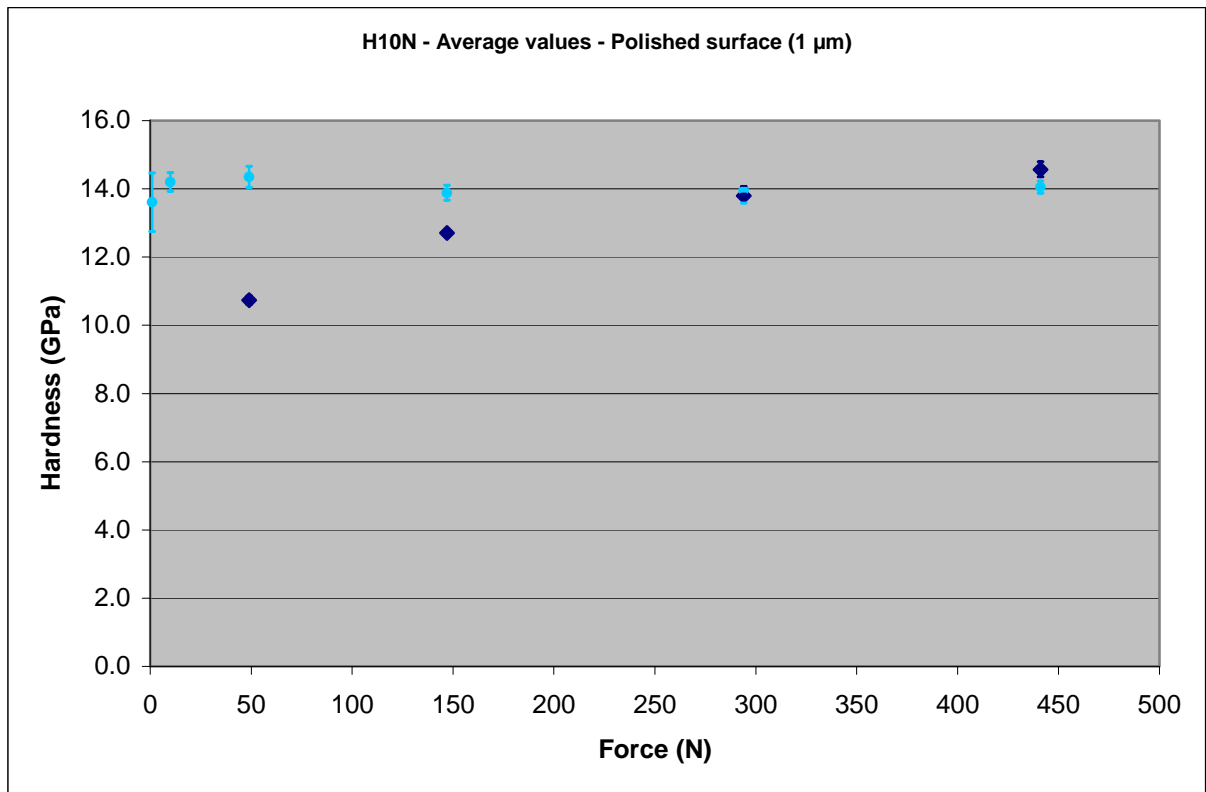


Figure 4.11: The measured hardness for different forces with a pyramidal indenter.



◆ Conical (120°) indenter ● Pyramide (136°) indenter

Figure 4.12: Comparison of measured hardness for Wolfram Carbide (H10N) with different indenters.

Notice from figure 4.7 and 4.10 that the difference between the cut surfaces and the polished surfaces are not very large. Thus in situ measurements of hard cores should give reliable results. Also observe from figure 4.8 that the conical indenter approaches an almost constant level somewhat below the pyramidal results for forces above 500 N. The reason for the low values for the conical indenter for small forces is that the conical indenter is not quite conical. The top of the cone has a more spherical form with a large radius of curvature compared to the much more pointed pyramid (figure 3.1, 3.2 and 3.3). Thus the results for the cone should stay below the pyramidal results, while approaching asymptotically the same results for large forces. The conical results become closer to the pyramidal results for large forces, but we are not quite sure that we reach the same level of hardness for large forces. We have not been able to test this for the Wolfram Carbide specimen since we could destroy the indenter when using larger forces (>500 N).

The pyramidal result reaches the steady state value for small forces around 10 N, although 1 N also could be used tentatively. The top of the pyramid is rather pointed. Thus it follows that the pyramidal form is applicable for microhardness measurements on small areas.

There is a slightly downward bend on the asymptotic part of the hardness curves (figure 4.7) for a load of 294 N when using the conical indenter. We speculate whether the reason for this is that fracture surfaces are created. It is observed that when the forces are higher than 150 N, cracks develop. They start along the surface of the contact between the indenter and the specimen and diverge radially outwards for the conical indenter (see figure 4.2, 4.3). The hypothesis is not supported by the results of the H10N hardcore in figure 4.10. H10N does not

show any such decrease in the hardness for the conical indenter. Instead it is observed that the hardness of the H10N hardcore do not reach a steady level when using the conical indenter.

The von Mises stress and the shear modulus of the G15 hardcore were found from a simple compression test [12], to read

$$Mis(e_{eff}) = \begin{cases} \frac{7.188 \cdot 10^{11} e_{eff}}{1 + 723.8 e_{eff}^{1.5}} Pa & \text{if } e_{eff} \leq 0.01969 \\ 4.72 \cdot 10^9 Pa & \text{if } e_{eff} \geq 0.01969 \end{cases}, G = 2.39 \cdot 10^{11} Pa, \nu = 0.2 \quad (3.1)$$

Using the equation set in (2.29) the different stresses as a function of the relative radial distance are given by figures 4.11-4.15.

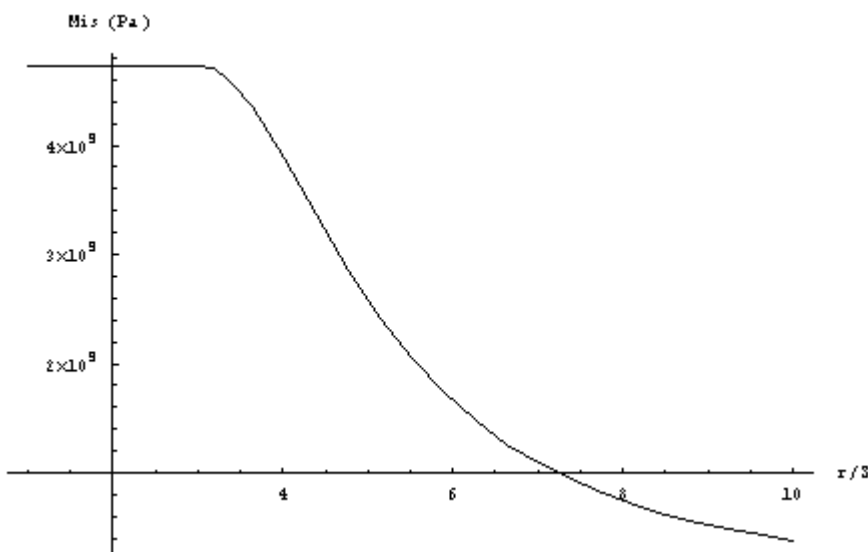


Figure 4.11: The theoretical von Mises stress during indentation as a function of the scaled distance from the surface of the indenter.

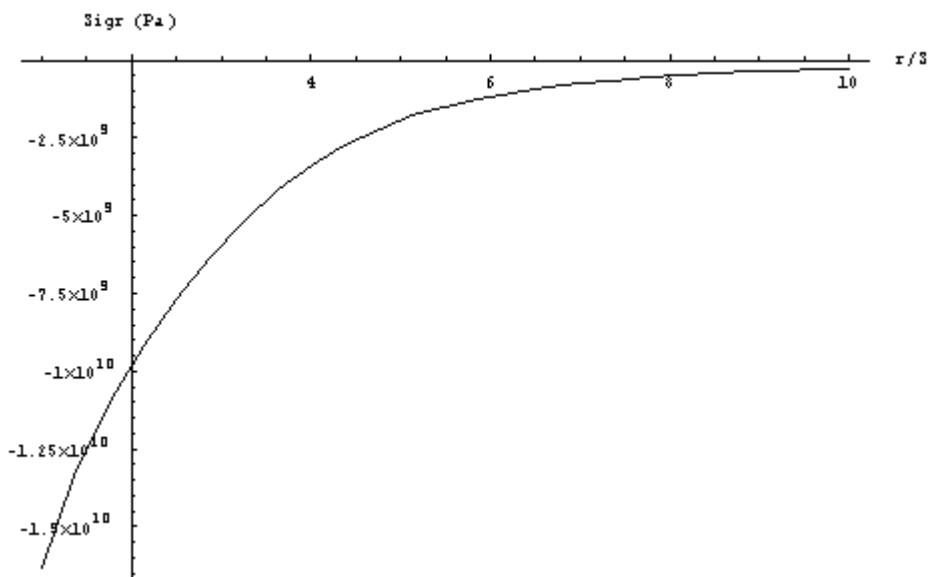


Figure 4.12: The theoretical radial stress as a function of the scaled distance.

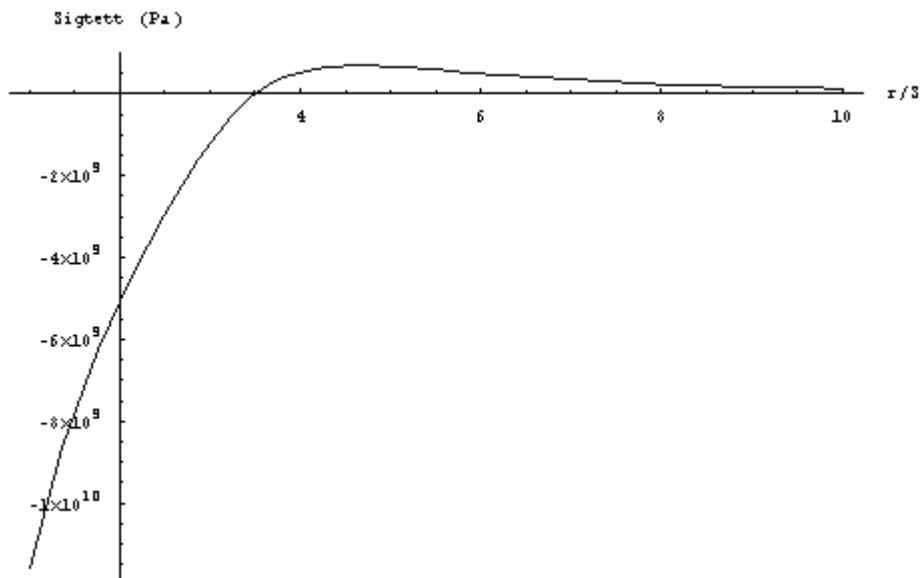


Figure 4.13: The theoretical circumferential stress as a function of the scaled distance.

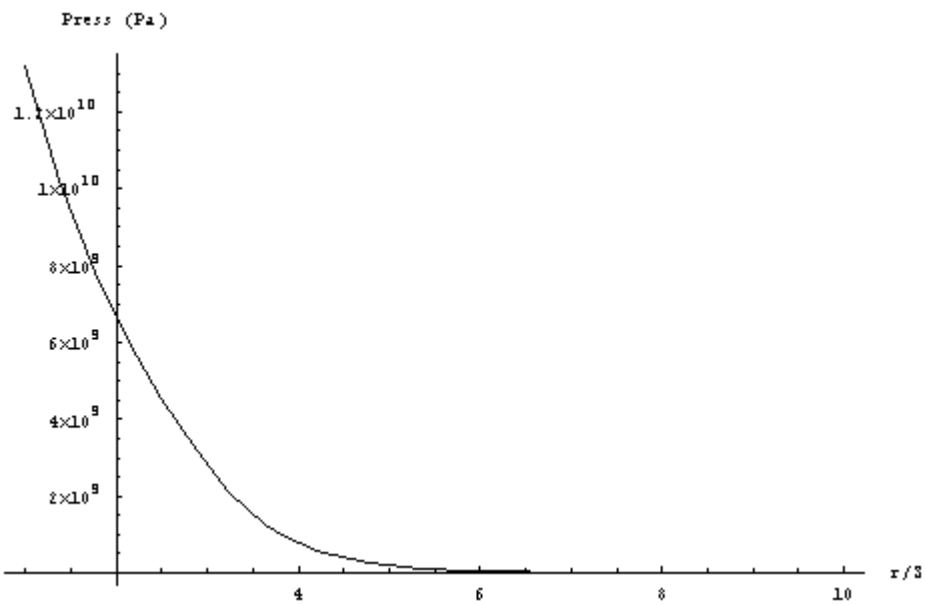


Figure 4.14: The theoretical pressure as a function of scaled distance.

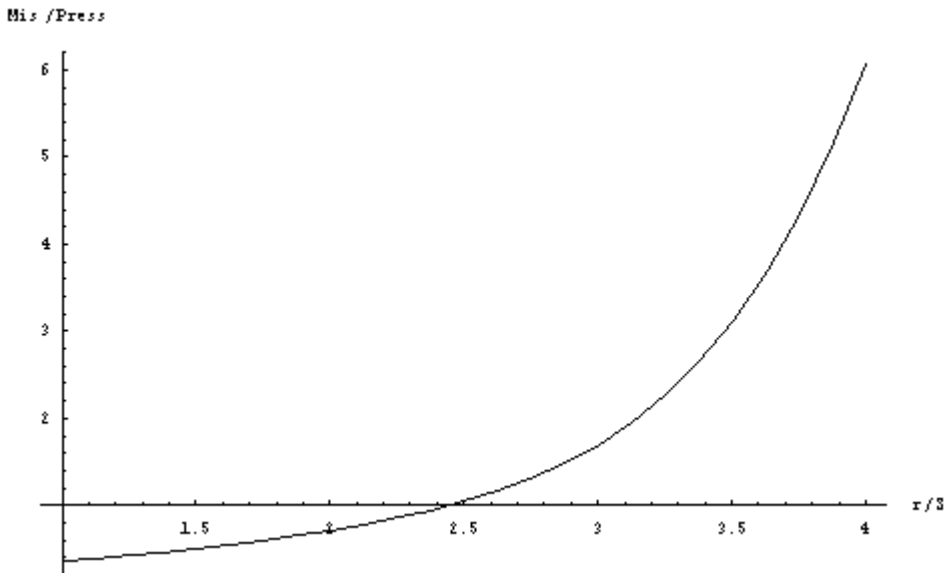


Figure 4.15: The theoretical fraction (von Mises stress/pressure) as a function of scaled distance.

The theoretical hardness is the radial stress at $r/S=1$, i.e. 17.0 GPa. This value is higher than the experimental value of 14.6 GPa for the pyramidal indenter and 14.0 GPa for the conical indenter. The reason for the discrepancy is uncertain but we believe that some changes have to be performed on the cavity theory.

5 HARDNESS TEST OF ARMOX 370 STEEL

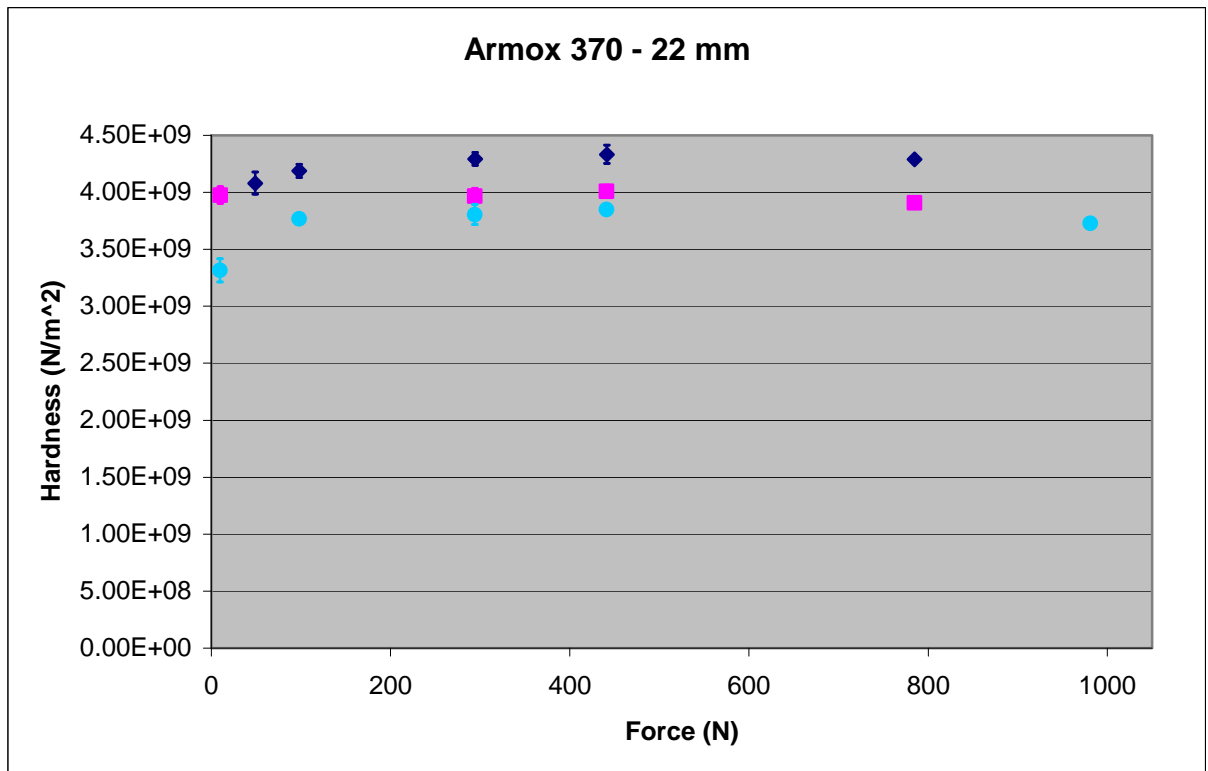
The 20 mm ArmoX 370 was cut and a tension test was performed on the specimen. It was found

$$Mis(e_{eff}) = Interpolation \left[\begin{array}{l} \{ \{0, 1.110^9 Pa\}, \{0.05, 1.19 \cdot 10^9 Pa\}, \{0.11, 1.22 \cdot 10^9 Pa\}, \{0.2, 1.25 \cdot 10^9 Pa\}, \\ \{0.4, 1.3 \cdot 10^9 Pa\}, \{0.6, 1.33 \cdot 10^9 Pa\}, \{0.8, 1.37 \cdot 10^9 Pa\}, \{1.0, 1.4 \cdot 10^9 Pa\}, \\ \{2.0, 1.58 \cdot 10^9 Pa\}, \{3.5, 1.81 \cdot 10^9 Pa\} \} \end{array} \right],$$

$$G = 7.92 \cdot 10^{10} Pa, \nu = 0.3$$

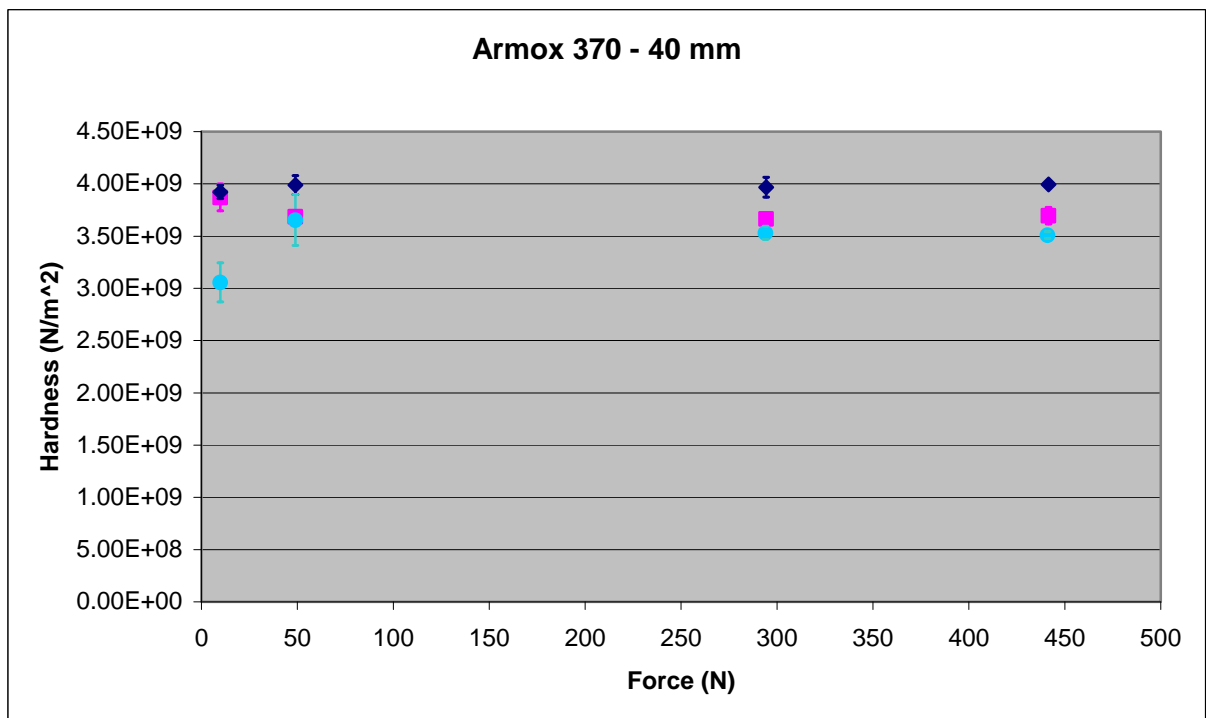
(4.1)

The hardness was measured to be approximately 4.0 GPa for the pyramidal indenter and 3.8 GPa for the conical indenter, while the equation set in (2.19) gives 4.7 GPa. Again the cavity theory overestimates the hardness (approximately 20% for both the Wolfram Carbide and the armor steel).



● Conical (120°) indenter ■ Pyramide (136°) indenter ◆ Pyramide (90°) indenter

Figure 4.1: The measured hardness for Armox 370 with plate thickness of 22 mm.



● Conical (120°) indenter ■ Pyramide (136°) indenter ◆ Pyramide (90°) indenter

Figure 4.2: The measured hardness for Armox 370 with plate thickness of 40 mm.

We generally find the same kind of relations as for the Wolfram Carbide. The theoretical value of the hardness is larger than the experimental value, and the hardness are found experimentally to be dependent of the form of the indenter.

6 HARDNESS TEST OF THE HUMAN SKULL

A piece of the skull from a human being was examined to find material properties. The hardness was measured. Figure 6.1 shows the results. A clear lowering of the hardness with the force was found. We have so far not found any good explanation for this phenomenon.

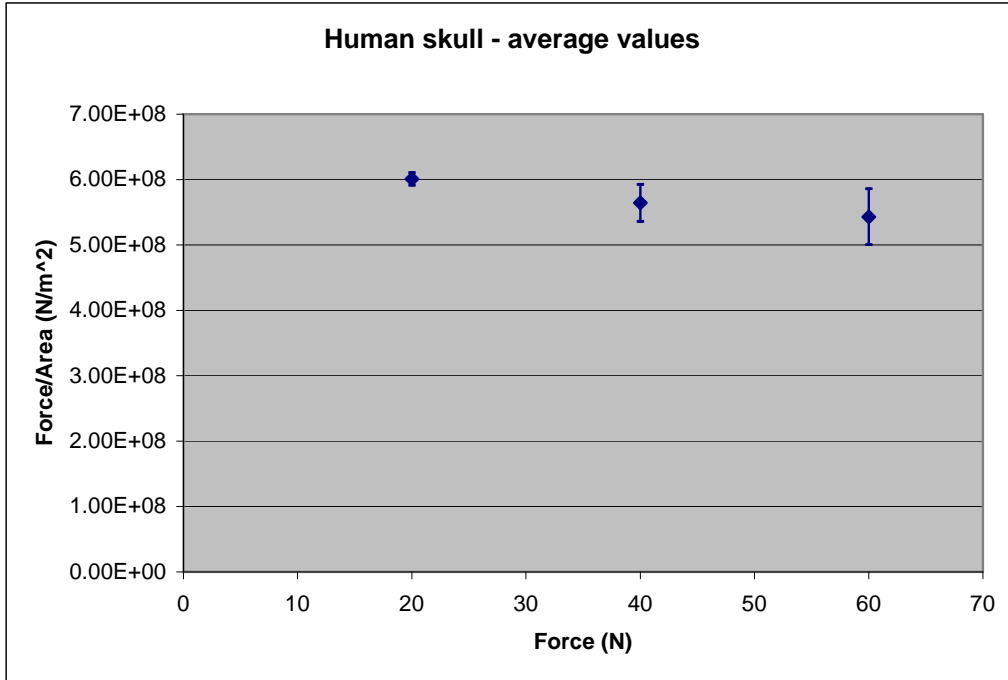


Figure 6.1: The hardness of the human skull. Pyramidal indenter (136°).

7 HARDNESS TEST OF JACKETS OF PROJECTILES

The hardness of jackets of 12.7 mm projectiles was studied. Figure 7.1 shows the jacket and where the hardness tests were conducted. Hardness test was made with a conical indenter (Rockwell) and a load of 30 kg.



At the surface in the rear part of jacket.

Figure 7.1: The jacket of a 12.7 mm projectile.

FN		
No.	Diameter [μm]	Force/Area [N/m^2]
1	566	1.17E+09
2	547	1.25E+09
3	541	1.28E+09
4	531	1.33E+09
5	545	1.26E+09
6	543	1.27E+09
7	530	1.33E+09
8	541	1.28E+09
9	558	1.20E+09
10	545	1.26E+09
Mean	545	1.26E+09
Std. Dev.	11	4.99E+07

P98		
No.	Diameter [μm]	Force/Area [N/m^2]
1	545	1.26E+09
2	545	1.26E+09
3	543	1.27E+09
4	549	1.24E+09
5	541	1.28E+09
6	551	1.23E+09
7	541	1.28E+09
8	551	1.23E+09
9	552	1.23E+09
10	545	1.26E+09
Mean	546	1.26E+09
Std. Dev.	4	1.91E+07

Table 7.1a: The hardness of the FN jacket. Table 7.1b: The hardness of the P98 jacket.

P53		
No.	Diameter [μm]	Force/Area [N/m^2]
1	547	1.25E+09
2	549	1.24E+09
3	549	1.24E+09
4	551	1.23E+09
5	547	1.25E+09
6	537	1.30E+09
7	535	1.31E+09
8	534	1.31E+09
9	541	1.28E+09
10	549	1.24E+09
Mean	544	1.27E+09
Std. Dev.	7	3.06E+07

Table 7.1c: The hardness of the P53 jacket.

In addition the hardness of the tip of the projectiles was measured. Here a Vickers indenter (pyramidal (136°)) was used with a load of 0.3 kg.

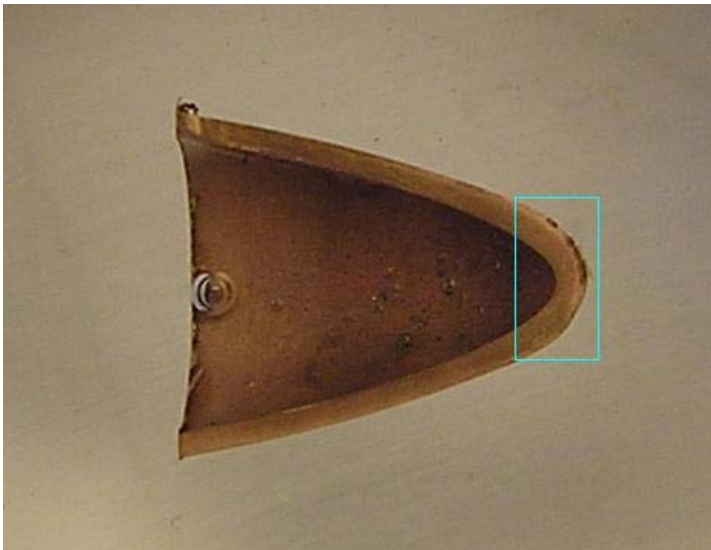


Figure 7.2: The cross-section of the tip of the jacket where the hardness tests was performed.

P98	
	Force/Area [N/m ²]
1	1.53E+09
2	1.56E+09
3	1.48E+09
Mean	1.52E+09
Std.dev.	3.72E+07

Table 7.2a: Hardness measurements of the tip of the jacket.

FN	
	Force/Area [N/m ²]
1	1.64E+09
2	1.48E+09
3	1.58E+09
Mean	1.57E+09
Std.dev.	7.71E+07

Table 7.2b: Hardness measurements of the tip of the jacket.

P53	
	Force/Area [N/m ²]
1	1.64E+09
2	1.75E+09
3	1.81E+09
Mean	1.73E+09
Std.dev.	8.96E+07

Table 7.2c: Hardness measurements of the tip of the jacket.

The difference in the hardness on the surface of the jackets was insignificant. For the tip region P98 and FN seems to have the same hardness. The hardness of the tip of P53 is somewhat larger.

8 CONCLUSION/DISCUSSION

In this report a study of the hardness of different materials is performed theoretically and experimentally. The main objective was to establish relations that can be used to construct constitutive material models. We apply the famous cavity theory for rigid penetration to the hardness test, and also expand the theory to include compressibility and strain hardening. For a conical indenter with a small spherical tip, we find that for small forces where the scale of the indentation dent is smaller or of the same order of magnitude as the radius of curvature the spherical tip, the cavity theory gives results far above the experimental values. For larger forces, where the scale of the indentation is much larger than the radius of curvature of the tip, the experimental results are in reasonably good agreement with the experimental results. But in general for large forces the theoretical hardness calculated by using the cavity theory overestimates the hardness with approximately 20% -30 % for our types of indenters. The reason for the discrepancy is uncertain. We can not completely rule out that the stress-strain curve used to calculate the theoretical hardness is somewhat too large, but we believe that

some changes have to be performed on the cavity theory even for large indentation forces. Finally, we find experimentally, and contrary to the cavity theory, that the hardness depends somewhat on the geometrical shape of the indenter.

In general we find that the material data from hardness tests can be used as an important input to the construction of constitutive models. There is a unique mapping from the stress-strain curve during simple compression to the hardness, but not the opposite. The reason for this is that the hardness follows from the integral of the stress-strain curve.

In further research we will study whether the hardness test and the fracture pattern around the indentation dent can be used for the construction of fracture models.

References

- 1: O'Neill H., "Hardness of Metals and Its Measurements", Sherwood Press, Cleveland, 1934
- 2: Williams R., "Hardness and Hardness Measurements", American Society for metals, Cleveland, 1934
- 3: Smith G.V., "Strain Hardening-Effects of Alloying Elements and Microstructure", from Cold Working of Metals, American Society for Metals, Cleveland, 1949
- 4: Lazarev P., "Relationships Between Hardness and Properties of the Elements", Bulletin, Academy of Sciences, Russia, Vol. 6, 1918, p. 1259; *ibid* 1918, p. 2241; *ibid* 1919, p. 1005
- 5: Innes J., "Mechanics of Solidity", Nature, Vol. 1006, 1921, p. 377
- 6: Benedicks C., "Derivation of Planck's Energy Distribution Law from the Agglomeration Hypothesis"; A Simple Relation Between Hardness and Vibration Frequency", *Annalen der Physik*, Vol. 42, 1913, p. 133
- 7: Kuznetzow V. D., "Mechanical Properties as a function of the Ionic Radii", *Journal of Physical Chemistry, USSR*, Vol. 6, 1935, p. 133
- 8: Westbrook J. H., "Temperature Dependence of the Hardness of Pure Metals", Thirty-fourth Annual convention of the American Society for Metals, March, p. 221-248, 1952
- 9: Tabor D., "The Hardness of Metals", Oxford Classic Texts in the Physical Sciences, Oxford University Press, 2002.
- 10: Janitzky E.J. and Baeyertz M., "The Marked Similarity in the Tensile Properties of several Heat Treated SAE Steels", *Metals Handbook*, American Society for Metals, Cleveland, 1939, p. 515
- 11: Moxnes J.F. and Frøyland Ø., "Simple Compression Studies of Wolfram Carbide", FFI/Report-2006/01922
- 12: Moxnes J.F. and Frøyland Ø., "Mechanical Studies of Wolfram Carbide", FFI/Report-2004/3860
- 13: Moxnes J.F. and Frøyland Ø., "Tensile Experiments of Wolfram Carbide", FFI/Report, in-press.

Appendix A

Hardness measurements for the Wolfram Carbide hardcores in the 12,7 mm MP projectiles.

G15 - Conical diamond indenter (60° half angle) – Polished surface (1 μm)								
	Load (N)							
	49		147		294		441	
	Diameter [μm]	Hardness [GPa]	Diameter [μm]	Hardness [GPa]	Diameter [μm]	Hardness [GPa]	Diameter [μm]	Hardness [GPa]
1	75.5	10.9	116.2	13.9	166.6	13.5	196.3	14.6
2	76.7	10.6	115.1	14.1	166.6	13.5	198.2	14.3
3	76.3	10.7	115.4	14.1	164.7	13.8	198.9	14.2
4	75.5	10.9	115.4	14.1	163.4	14.0	197.6	14.4
5	75.7	10.9	115.3	14.1	164.0	13.9	198.9	14.2
Average	75.9	10.8	115.5	14.0	165.1	13.7	198.0	14.3
Std. Dev.	0.5	0.2	0.4	0.1	1.5	0.2	1.1	0.2

G15 - Conical diamond indenter (60° half angle) - Cut surface								
	Load (N)							
	49		147		294		441	
	Diameter [μm]	Hardness [GPa]	Diameter [μm]	Hardness [GPa]	Diameter [μm]	Hardness [GPa]	Diameter [μm]	Hardness [GPa]
1	73.4	11.6	116.8	13.7	166.5	13.5	201.5	13.8
2	74.9	11.1	116.8	13.7	167.1	13.4	200.8	13.9
3	71.3	12.3	117.6	13.5	165.8	13.6	202.8	13.7
4	74.7	11.2	118.0	13.4	170.4	12.9	204.7	13.4
5	77.2	10.5	115.7	14.0	167.8	13.3	205.4	13.3
Average	74.3	11.3	117.0	13.7	167.5	13.3	203.0	13.6
Std. Dev.	2.2	0.7	0.9	0.2	1.8	0.3	2.0	0.3

G15 - Pyramidal diamond indenter (136° angle between faces) - Polished surface (1 μm)								
	Load (N)							
	49		147		294		441	
	Diagonal [μm]	Hardness [GPa]	Diagonal [μm]	Hardness [GPa]	Diagonal [μm]	Hardness [GPa]	Diagonal [μm]	Hardness [GPa]
1	82.6	14.4	142.5	14.5	202.6	14.3	247.4	14.4
2	82.9	14.3	139.7	15.1	200.7	14.6	247.4	14.4
3	81.2	14.9	140.9	14.8	201.4	14.5	246.8	14.5
4	82.3	14.5	141.6	14.7	202.6	14.3	246.8	14.5
5	81.6	14.7	142.8	14.4	200.7	14.6	246.2	14.6
Average	82.1	14.5	141.5	14.7	201.6	14.5	246.9	14.5
Std. Dev.	0.7	0.3	1.3	0.3	1.0	0.1	0.5	0.1

H10N - Conical diamond indenter (60° half angle) - Cut surface								
	Load (N)							
	49		147		294		441	
	Diameter [μm]	Hardness [GPa]						
1	79.5	9.9	117.7	13.5	163.4	14.0	200.1	14.0
2	78.0	10.3	118.5	13.3	165.3	13.7	198.2	14.3
3	77.4	10.4	119.8	13.0	164.0	13.9	197.0	14.5
4	77.2	10.5	118.4	13.4	165.3	13.7	193.8	14.9
5	75.3	11.0	118.4	13.4	162.1	14.2	193.2	15.0
Average	77.5	10.4	118.6	13.3	164.0	13.9	196.5	14.6
Std. Dev.	1.5	0.4	0.8	0.2	1.4	0.2	2.9	0.4

H10N - Conical diamond indenter (60° half angle) – Polished surface (1 μm)								
	Load (N)							
	49		147		294		441	
	Diameter [μm]	Hardness [GPa]						
1	75.8	10.9	121.5	12.7	165.9	13.6	195.7	14.7
2	77.0	10.5	120.8	12.8	165.9	13.6	195.1	14.8
3	76.2	10.7	121.3	12.7	164.7	13.8	195.7	14.7
4	76.0	10.8	121.9	12.6	162.8	14.1	196.3	14.6
5	76.2	10.7	121.3	12.7	164.4	13.9	198.9	14.2
Average	76.2	10.7	121.4	12.7	164.7	13.8	196.3	14.6
Std. Dev.	0.5	0.1	0.4	0.1	1.3	0.2	1.5	0.2

H10N - Pyramidal diamond indenter (136° angle between faces) - Polished surface (1 μm)												
	Load (N)											
	1		10		49		147		294		441	
	Diagonal [μm]	Hardness [GPa]										
1	11.6	14.9	37.5	14.2	83.2	14.2	146.3	13.7	205.8	13.9	248.1	14.3
2	12.1	13.7	37.9	13.9	84.0	13.9	146.0	13.8	205.8	13.9	250.6	14.0
3	12.5	12.8	37.3	14.4	81.9	14.6	146.6	13.7	205.8	13.9	252.5	13.8
4	12	13.9	37.1	14.5	82.1	14.5	145.0	14.0	205.1	14.0	250.6	14.0
5	12.5	12.8	37.9	13.9	82.1	14.5	143.8	14.2	203.9	14.1	251.2	14.0
Average	12.1	13.6	37.5	14.2	82.7	14.3	145.5	13.9	205.3	14.0	250.6	14.0
Std. Dev.	0.4	0.9	0.4	0.3	0.9	0.3	1.1	0.2	0.8	0.1	1.6	0.2

Hardness measurements on bones from the human skull.

Vickers diamond indentation - 20 N

	Diagonal [μm]	HV20	Force/Area [N/m^2]
1	255,7	58	6,12E+08
2	258,9	56	5,97E+08
3	259,5	56	5,94E+08
Average	258,0	57	6,01E+08
Std.dev.	2,0	1	9,57E+06

Vickers diamond indentation - 40 N

	Diagonal [μm]	HV20	Force/Area [N/m^2]
1	387,7	50	5,32E+08
2	370	55	5,84E+08
3	372,5	54	5,77E+08
Average	376,7	53	5,64E+08
Std.dev.	9,6	3	2,81E+07

Vickers diamond indentation - 60 N

	Diagonal [μm]	HV20	Force/Area [N/m^2]
1	451,2	56	5,89E+08
2	487,2	48	5,06E+08
3	473,9	51	5,34E+08
Average	470,8	51	5,43E+08
Std.dev.	18,2	4	4,26E+07

Hardness measurements on armor steel plates.

Armox 370 - 22 mm - Conical diamond indenter										
	Load (N)									
	9.8		98		294		441		981	
	Diameter [μm]	Force/Area [GPa]								
1	60.5	3.41	182.6	3.75	316	3.74	380	3.89	580	3.72
2	62.4	3.21	182.2	3.76	315	3.77	384	3.82	581	3.70
3	61.3	3.32	181.5	3.79	310	3.91	383	3.84	576	3.77
Average	61.4	3.31	182.1	3.77	313.7	3.80	381.9	3.85	578.9	3.73
Std. Dev.	1.0	0.10	0.6	0.02	3.6	0.09	2.0	0.04	2.9	0.04

Armox 370 - 22 mm - Pyramidal indenter (136°)								
	Load (N)							
	10		294		441		785	
	Diagonal [μm]	Force/Area [GPa]						
1	70.9	3.98	389	3.89	471	3.99	635	3.90
2	71.6	3.90	383	4.02	472	3.97	633	3.92
3	70.3	4.05	384	3.98	466	4.07	634	3.91
Average	70.9	3.98	385	3.97	469	4.01	634	3.91
Std. Dev.	0.7	0.07	3	0.07	3	0.05	1	0.01

Armox 370 - 22 mm - Pyramidal indenter (90°)										
	Load (N)									
	49		98		294		441		785	
	Diagonal [μm]	Force/Area [GPa]								
1	156	4.05	215	4.25	369	4.33	451	4.34	603	4.32
2	158	3.95	217	4.18	371	4.28	446	4.44	605	4.28
3	153	4.17	218	4.14	368	4.35	454	4.28	607	4.27
4	154	4.14			374	4.22	455	4.27		
Average	156	4.06	216	4.19	369	4.32	450	4.35	605	4.29
Std. Dev.	2	0.11	1	0.06	1	0.03	4	0.08	2	0.03

Armox 370 - 40 mm - Pyramidal indenter (136°)								
	Load (N)							
	9.81		49		294		441	
	Diagonal [μm]	Force/Area [GPa]						
1	71.7	3.82	163	3.70	401	3.66	487	3.72
2	69.9	4.02	163	3.70	401	3.66	485	3.76
3	72.1	3.77	164	3.65	401	3.67	495	3.61
Average	71.2	3.87	163	3.68	401	3.66	489	3.70
Std. Dev.	1.2	0.13	1	0.03	0	0.00	5	0.08

Armox 370 - 40 mm - Pyramidal indenter (90°)								
	Load (N)							
	9.81		49		294		441	
	Diagonal [μm]	Force/Area [GPa]	Diagonal [μm]	Force/Area [GPa]	Diagonal [μm]	Force/Area [GPa]	Diagonal [μm]	Force/Area [GPa]
1	71.4	3.85	156	4.03	385	3.98	469	4.02
2	70.3	3.97	156	4.05	381	4.05	470	4.00
3	70.5	3.95	159	3.89	390	3.87	472	3.97
Average	70.7	3.92	156.9	3.99	385.3	3.97	470.0	4.00
Std. Dev.	0.6	0.06	1.8	0.09	4.6	0.09	1.4	0.02

Armox 370 - 40 mm - Conical diamond indenter								
	Load (N)							
	9.8		49		294		441	
	Diameter [μm]	Force/Area [GPa]	Diameter [μm]	Force/Area [GPa]	Diameter [μm]	Force/Area [GPa]	Diameter [μm]	Force/Area [GPa]
1	64.5	3.00	126	3.93	323	3.59	402	3.47
2	63.4	3.26	134	3.50	326	3.51	399	3.54
3	65.6	2.90	133	3.52	328	3.47	400	3.51
Average	64.5	3.06	130.9	3.65	325.8	3.53	400.2	3.51
Std. Dev.	1.1	0.19	4.2	0.24	2.8	0.06	1.9	0.03

Appendix B

Assume as an example that the material is elastic/plastic. It follows that

$$e_r = \varepsilon_r - (1/3)(\varepsilon_r + 2\varepsilon_\theta) = \varepsilon_r - \frac{(\sigma_r + 2\sigma_\theta)(1-2\nu)}{6G(1+\nu)} = \varepsilon_r + \frac{p(1-2\nu)}{2G(1+\nu)} \quad (B.1)$$

$$e_{eff} = -\frac{2}{3} \ln\left(1 - S(t)^3 / r^3\right) - \frac{(1-2\nu)Y \ln(2S(t)G/(Yr))}{3G(1+\nu)},$$

where we have inserted the pressure p from the incompressible solution. Solving for the elastic/plastic interface relation gives that

$$3Ge_{eff} = Y \Rightarrow -2GLn\left(1 - S(t)^3 / r^3\right) - \frac{(1-2\nu)YLn(2S(t)G/(Yr))}{(1+\nu)} = Y$$

$$s(t) = \frac{S(t)}{\left(1 - \text{Exp}\left[-\frac{Y\left(1+\nu+(1-2\nu)Ln\left(\frac{2G}{Y} \frac{S(t)}{s(t)}\right)\right)}{2G(1+\nu)}\right]\right)^{1/3}} \approx \left(\frac{2G(1+\nu)}{Y\left(1+\nu+(1-2\nu)Ln\left(\frac{2G}{Y} \frac{S(t)}{s(t)}\right)\right)}\right)^{1/3} S(t)$$

$$s(t) \approx \left(\frac{2G(1+\nu)}{Y\left(1+\nu+(2/3)(1-2\nu)Ln\left(\frac{2G}{Y}\right)\right)}\right)^{1/3} S(t)$$

(B.2)